ELSEVIER

Materials Science and Engineering A206 (1996) 71–80

MATERIALS SCIENCE & ENGINEERING A

Effect of Mo on microstructure and mechanical properties of TiC–Ni-based cermets produced by combustion synthesis–impact forging technique

J.C. LaSalvia[a], D.K. Kim[b], M.A. Meyers[a]

[a]*Institute for Mechanics and Materials, Department of Applied Mechanics and Engineering Sciences, University of California, San Diego, La Jolla, CA 92093-0411, USA*

[b]*Department of Ceramic Science and Engineering, Korea Advanced Institute of Science and Technology, Yusong Gu, Taejon 205-701, South Korea*

Received 6 February 1995

Abstract

The effect of Mo additions on the microstructure and mechanical properties of TiC–30 wt.% Ni cermets produced by the combustion synthesis–impact forging technique was investigated. The Mo content was varied between 0 and 10 wt.%, in 2 wt.% increments. Cylindrical tiles 6.35 cm in diameter and 1.27 cm thick were produced with apparent densities above 99%. Microscopically, the addition of Mo resulted in a decrease in the number of microstructural defects such as interphase debonding and binder microcracking. The microstructure consisted of a spheroidal carbide phase with a high degree of contiguity (decreasing with increasing Mo content). The Mo additions did not have a profound effect on the carbide phase morphologies (faceted vs. spheroidal), mean apparent particle diameters (3.5 μm–4.5 μm), or particle size distribution. Energy-dispersive X-ray analysis revealed Mo preferentially in the carbide phase, with trace amounts in the Ni alloy binder. A significant amount of Ti was found in solution with Ni. Vickers' microhardness did not vary significantly with Mo content and was approximately 13 GPa. Compressive strength, transverse rupture strength, fracture toughness, and Young's moduli increased with increasing Mo content; the mean values for the 8 wt.% Mo material were approximately 3400 MPa, 1300 MPa, 22 MPa $m^{1/2}$, and 340 GPa respectively. The beneficial effect of Mo is due to the improved wettability of the Ni alloy binder on the carbide phase. Improved wettability results in a decrease in detrimental microstructural defects and an increase in the interphase bond strength and phase uniformity.

Keywords: Molybdenum; Microstructure; Mechanical properties

1. Introduction

Combustion synthesis or self-propagating high-temperature synthesis (SHS) is a process by which condensed phases are produced by self-sustaining exothermic chemical reactions. One of the unique characteristics of combustion synthesis is that the reactions are self-propagating: once the reaction is initiated within one part of a reactive mixture, it readily propagates into the surrounding mixture. The reaction is manifested as a combustion wave. Many industrially important materials such as borides, carbides, cermets, intermetallics, nitrides, silicides, and composites have been produced by this process [1–5].

While it was recognized at the turn of the century that thermite reactions are self-propagating [6], the contemporary research activity in this area was initiated by Merzhanov, Borovinskaya, and coworkers [5] in the USSR, during the late 1960s and early 1970s. They have been able to produce approximately 500 different materials, with many being produced on an industrial level [7]. Reviews on combustion synthesis have been made by Crider [1], Frankhouser et al. [2], Munir and Anselmi-Tamburini [3], Yi and Moore [4], and Merzhanov [5].

One of the main disadvantages of using combustion synthesis to produce structural engineering parts in a single-step process is that the resulting parts are typically porous (with the exception of SHS castings). Fig.

0921-5093/96/$15.00 © 1996 — Elsevier Science S.A. All rights reserved

1 is an optical micrograph obtained from a TiC–30Ni–14Mo (weight per cent) material produced by combustion synthesis (dark areas are residual porosity). The factors which contribute to the residual porosity include initial green body porosity, lower specific volume of the product phase, and outgassing of volatilized impurities. Because of the large amount of transient liquid phase during the reaction, the porosity represents the failure of transient liquid phase sintering mechanisms to successfully densify the body [8].

A number of methods have been used to densify the porous materials during or after the combustion synthesis process, while the material still exists in a ductile state. In Russia and China, quasi-isostatic hot pressing has been successfully used to produce dense plates of large size [9,10]. Furthermore, extrusion, rolling, and explosive compaction have been developed [11–13]. $MoSi_2$ heating elements have been produced utilizing extrusion [11]. In Japan, pressure-assisted reactive sintering has been successfully used [14,15]. In the US, pressureless and pressure-assisted reactive sintering, conventional and quasi-isostatic hot pressing, impact forging, and explosive compaction have been successfully used to obtain dense materials [16–26].

LaSalvia et al. [20] introduced the impact forging technique to produce cylindrical TiC tiles 10 cm in diameter and 1 cm thick with apparent densities above 99%. Hoke et al. [21] were able to produce TiB_2 tiles 8.5 cm in diameter and 1 cm thick with densities above 96% of the theoretical. More recently, high density (above 96% of the theoretical) TiC–Ni cermets [22] and TiB_2–SiC composites [23] were produced. Fig. 2(a) is a backscattered electron micrograph of a TiC–30Ni cermet obtained using this technique. As can be seen, the microstructure consists of a spheroidal TiC phase (some faceting) embedded in an Ni alloy binding phase. The high degree of contiguity of the TiC phase indicates a less than optimum arrangement of phases which leads to a degradation of mechanical properties. Humenik and Parikh [27,28] investigated the wettability enhance-

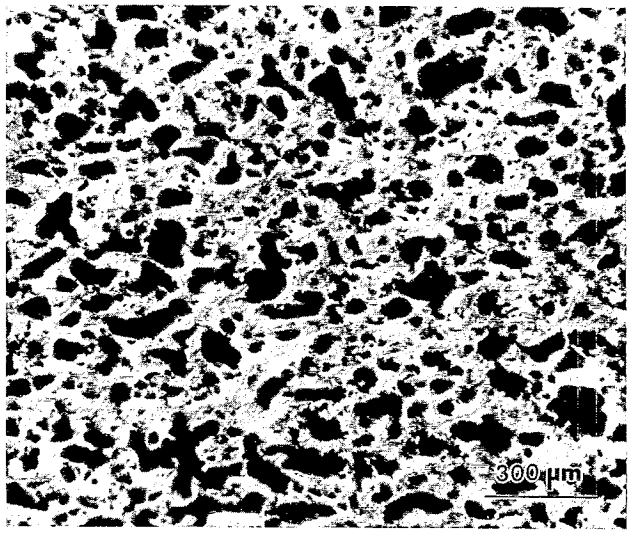

Fig. 1. Optical micrograph obtained from a TiC–30Ni–14Mo combustion synthesized compact.

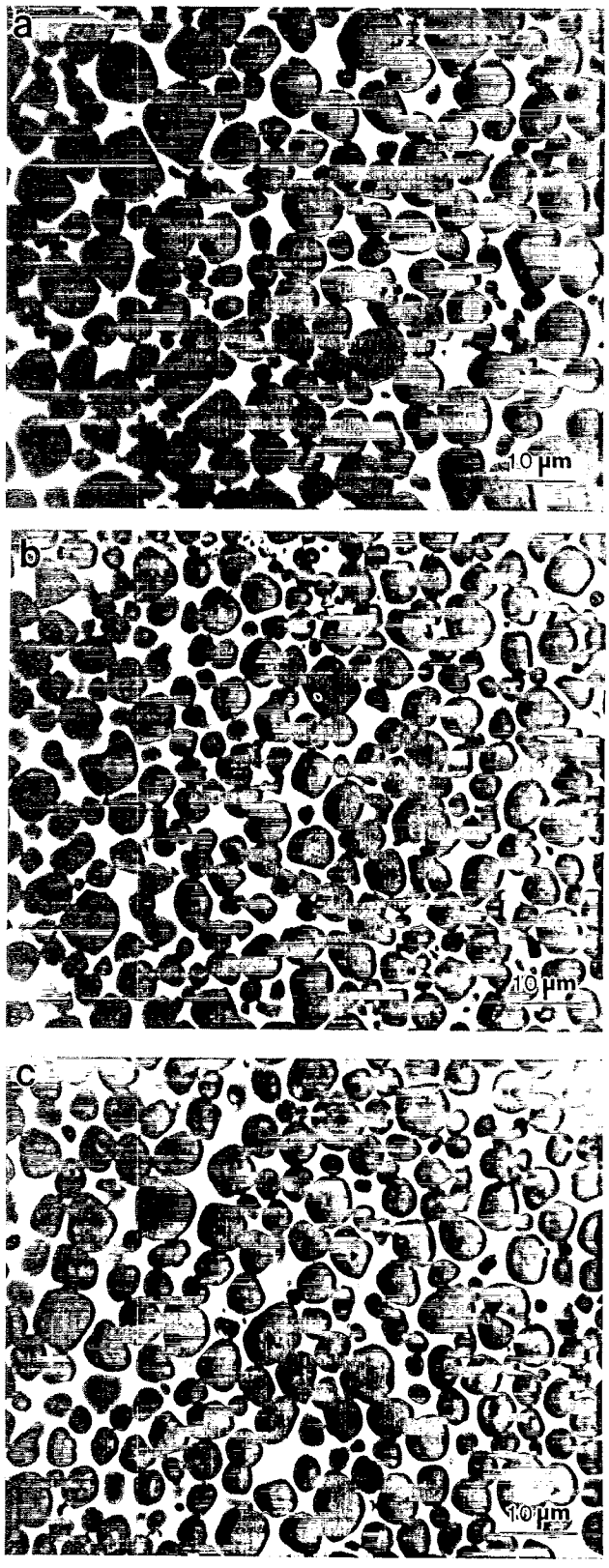

Fig. 2. Backscattered electron micrographs for combustion synthesized–impacted forged (a) 0 Mo, (b) 4 Mo, and (c) 8 Mo.

ment of Ni melts on TiC by introducing alloy additions and observed that replacing 10 wt.% of the Ni binder with Mo resulted in complete wetting (i.e. contact angle goes to 0°). As a result, both TiC particle coarsening and contiguity were substantially decreased. This improvement in the microstructure also resulted in an improvement in mechanical performance which led to industrial use [29–33].

The purpose of this investigation is to determine the effect of Mo additions on the microstructures and mechanical properties of TiC–Ni-based cermets produced by the combustion synthesis–impact forging technique. Because of the possible wide variations in compositions, the Ni content was fixed at 30 wt.%, while the Mo content was varied between 0 and 10 wt.% increments.

2. Experimental procedures

High purity (99.7%) Ti (Micron Metals Inc., Salt Lake City, UT), (99.9%) C in graphite form (Consolidated Astronautics, Smithtown, NY), (99.5%) Ni (Aldrich Chemical Co., Milwaukee, WI), and (99.9%) Mo (Cerac/Pure Division, Milwaukee, WI) powders were used in this investigation. The Ti, C, Ni, and Mo powder sizes were less than 44 μm (−325 mesh), 2 μm, 3 μm, and 2–4 μm respectively.

The powders (400 g batches) were dry mixed in a polyethylene bottle under an Ar atmosphere for 24 h using a grinding medium (2:1 mass ratio). After mixing, the powder was placed into a vacuum oven (100 mm Hg, 100 °C) for 24 h to remove any absorbed water. Green cylindrical tiles 6.35 cm in diameter and approximately 2.3 cm thick (about 220 g) with densities of 65% of the theoretical were produced by compacting in a steel die using a compaction pressure of 55 MPa.

Details of the combustion synthesis–impact forging technique (i.e. procedures and equipment) are given elsewhere [20–22]. Of critical importance in this technique is the time delay between the initiation of the combustion synthesis process and densification. The issues of reaction completion, composition evolution, and material ductility determine the extent of this time delay. Preliminary experiments showed that a time delay between 8 and 15 s yields fully reacted dense compacts. A time delay of 20 s resulted in a fully dense compact with macrocracks. In this investigation, a time delay of 15 s was used.

Densified disks were sectioned for metallographic, scanning electron microscopy, elemental microanalysis, X-ray diffraction, and apparent density measurements. For a reliable comparison basis, specimens were taken from the central region of each disk. X-ray standards of high purity (Johnson Matthey, Seabrook, NH) Ti (99.99+%), Ni (99.994%), and Mo (99.95%) were used for semiquantitative X-ray microanalysis. Atomic number Z, absorption A, and fluorescence F corrections were not performed on the data. Particle size measurements using the linear-intercept technique were conducted with the aid of an image analyzer in which the number of measurements gave a 95% confidence level for the mean in the range less than ±5% of its value (1000 measurements per specimen).

Vickers' microhardness measurements (500 gf load) were conducted to examine the effect of Mo on hardness. Quasi-static compression and four-point bend tests were limited to the 0 Mo, 4 Mo, and 8 Mo materials. The top and bottom surfaces of the densified compacts were ground flat and parallel to within 5μm. Compression specimens with dimensions 4 mm × 4 mm × 7 mm and four-point bend specimens with dimensions 4 mm × 7 mm × 30 mm were cut from the ground compacts by electrodischarge machining. Both compression and four-point bend tests (a minimum of three experiments per test per material) were conducted using a screw-driven Instron compression–tension mechanical testing machine. The loading ends of the compression specimens were polished using 1 μm and 0.25 μm diamond pastes. This was done to eliminate the surface flaws introduced during flat grinding. During loading, two sets of load-bearing platens were used. These platens were ground flat and parallel to 15 μm. Initially, these platens were micrograined WC–6Co. In later tests, micrograined WC–10Co was used because the WC–6Co platens would often fail before the maximum load was reached. Stainless steel shims 25 μm thick were used between the specimen and the WC–10Co platens. The use of shims during the compression testing of cemented carbides is recommended by the ASTM under designation E9-87 [34]. Tests were conducted at a loading rate of 4 μm s^{-1}, which corresponded to a strain rate of approximately 5×10^{-3} s^{-1}. Alignment of the specimen and WC–10Co platens with the loading axis of the machine was performed by sight.

The four-point bend fixture used high carbon steel rods 3 mm in diameter as bottom simple supports and loading points. The bottom supports and loading points were 25.4 mm and 12.7 mm apart respectively. Tests were conducted at a loading rate of 4 μm s^{-1}.

The elastic moduli (Young's moduli, shear moduli, and Poisson's ratio) were determined using an ultrasonic technique in which both the longitudinal (p wave) and shear (s wave) wave speeds were measured [35]. Assuming that the materials are linear elastic, isotropic, homogeneous bodies, the Young's modulus E, shear modulus μ, and Poisson's ratio ν are related to the longitudinal C_L and the shear C_S wave speeds by the equations [36]

$$E = \frac{3C_L^2 - 4C_S^2}{C_L^2 - C_S^2}\rho C_S^2 \quad (1)$$

$$\mu = \rho C_S^2 \quad (2)$$

$$\nu = \frac{C_L^2 - 2C_S^2}{2(C_L^2 - C_S^2)} \quad (3)$$

3. Results and discussion

3.1. Microstructure

Qualitatively, the resulting combustion synthesis–impact forged microstructures do not appear to be very different; they consist of a spheroidal–faceted carbide phase embedded in a nearly continuous Ni alloy binding phase. Backscattered electron micrographs for the 0, 4, and 8 Mo materials are shown in Figs. 2(a), 2(b), and 2(c) respectively. The dramatic influence of Mo on the TiC particle size observed by Humenik and Parikh [27] is not obtained. This is due to the fact that the processing techniques are entirely different. Using the combustion wave arresting technique developed by Rogachev et al. [37], LaSalvia et al. [38] showed that the microstructure develops by a continual process of dissolution and supersaturation of C in the Ti–Ni–C melt, heterogeneous nucleation and growth of a carbide overgrowth on the C particles, and break up of this overgrowth into carbide particles. Thus, the carbide particle size is not strongly dependent on the reactant particle sizes, but is determined by the thermal excursion, which is approximately the same for all specimens, since it is dictated by the scale and processing set-up.

Semiquantitative energy-dispersive X-ray microanalysis was conducted to determine the distribution of elements (with the exception of C) within the materials.

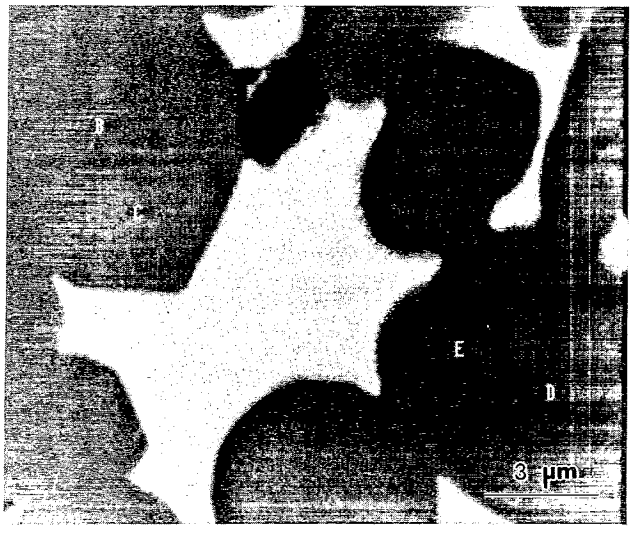

Fig. 3. Backscattered electron micrograph of 4 Mo material Letters indicate points where energy-dispersive X-ray microanalysis was conducted.

Table 1
Semiquantitative energy-dispersive X-ray microanalysis data for Fig. 3

Location point	Ti (%)	Ni (%)	Mo (%)
A	7	93	—
B	96	0.4	3.6
C	96	0.5	3.5
D	96	1	3
E	96	1	3
F	6	93.8	0.2

Fig. 3 is a backscattered electron micrograph taken from the 4 Mo material. X-ray samplings were taken at points A through F. Table 1 contains the results (in weight per cent). The percentages were normalized using counts from the thin foil standards of each element. As can be seen from this table, the Ni binder contains a small percentage of Ti and a very small percentage of Mo in solution. The majority of the Mo is found within the carbide phase (forming the (Ti,Mo)C complex carbide) which is characteristic of materials produced by conventional means [29–33]. The characteristic core–shell structure (i.e. Mo-poor and Mo-rich shell) for these materials is observed in a large number of particles (increasing with Mo content; see Fig. 2(c) for example); however, many particles also appear to have a uniform distribution of Mo, as shown for the particles in Fig. 3.

Fig. 4 shows the results of the particle size measurements. The error bars denote a 95% confidence level that the mean lies within ±5% of its specified value. The mean particle size for these materials ranges between 3.5 μm and 4.5 μm. Conventionally produced TiC-based cermets typically possess particle sizes between 1 μm and 2 μm. The conventional densification method is liquid phase sintering of the green compacts which initially consist of micron-size carbide particles. During sintering, the carbide particles coarsen as a result of dissolution–reprecipitation. Sintering temperatures for TiC-based cermets are typically around

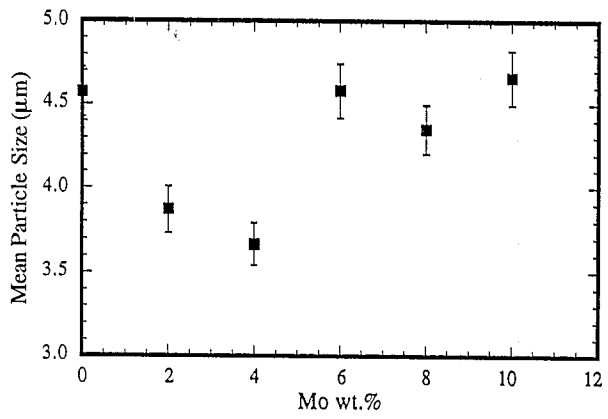

Fig. 4. Effect of Mo on the carbide particle size of combustion synthesized–impacted forged TiC–Ni-based materials.

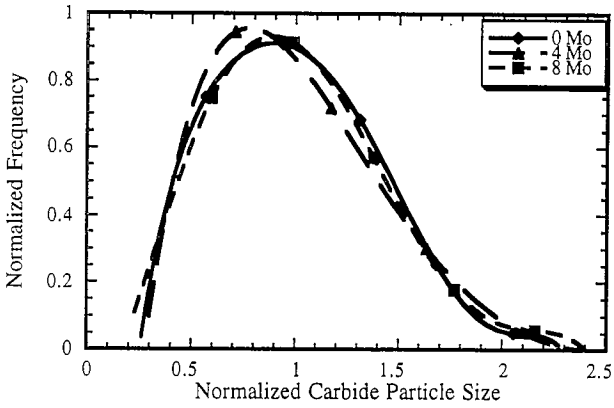

Fig. 5. Effect of Mo on the carbide particle size distribution.

1350 °C in order to minimize carbide particle coarsening [29–33]. The temperatures within the combustion wave greatly exceed this value ($T_{ad} = 2500$ °C); thus, a larger particle size would be expected assuming that the physical processes which govern the evolution of the microstructure during the combustion synthesis process do not deviate significantly from those occurring during conventional processing. LaSalvia et al. [38] observed that carbide particle coarsening does occur, with below 1 μm size particles coarsening to 3 μm size particles.

Fig. 5 shows the normalized fraction of carbide particle sizes vs. normalized particle size (with respect to the mean particle size) for the 0, 4, and 8 Mo materials. The curves are characteristic (i.e. broad distributions) of liquid phase sintered systems which have undergone some coarsening process [8]. Qualitatively, the shapes of 0 and 8 Mo curves are the same while that for the 4 Mo material is slightly shifted towards lower particle sizes. This shift is attributed to the slight morphological differences between the carbide phases in these materials.

Evidence for the incomplete solutionizing of Mo within the Ni alloy melt was observed. One such region found in the 2 Mo material is shown in Fig. 6. The mean size of these particles is approximately 1 μm. These particles exhibit a multiple core–shell structure. Some of the particles appear to have a structure which is the reverse of that expected (i.e. Mo-rich core and Mo-poor shell). These regions are due to Mo agglomerates which were not broken up and uniformly dispersed during the mixing process as shown by LaSalvia et al. [38]. Examination of both Ti and Ni reactant powders revealed agglomerates. However, during the reaction the temperature–time history is sufficient to ensure the complete melting of these powders. The formation of this Ti–Ni melt enhances the mixing of components which improves the composition homogeneity. The temperature–time history is not sufficient to melt or dissolve completely the largest Mo agglomerates (Mo melting temperature, about 2600 °C [39]). Ensuring that the Mo agglomerates are as small as possible and dispersed uniformly throughout the reactant powder mixture is extremely important for enhancing not only the composition homogeneity, but the macroscopic distribution of phases in the final product (owing to improved wettability of the liquid phase on the solid phase).

A decrease in the number of microstructural flaws such as voids, interphase debonding, and binder microcracks is observed with increasing Mo content. Fig. 7 shows typical flaws observed primarily within the 0 Mo material. Figs. 7(a), 7(b), and 7(c) show an area devoid of the Ni alloy binder, partial debonding between the Ni alloy binder and a TiC particle, and partial debonding between phases, as well as a microcrack penetrating into the Ni alloy binder, respectively. Both the interphase debonding and the microcracks within the Ni alloy binder are evidence that large residual tensile stresses existed within it. Newkirk and Sisler [40] conducted an investigation into the presence residual

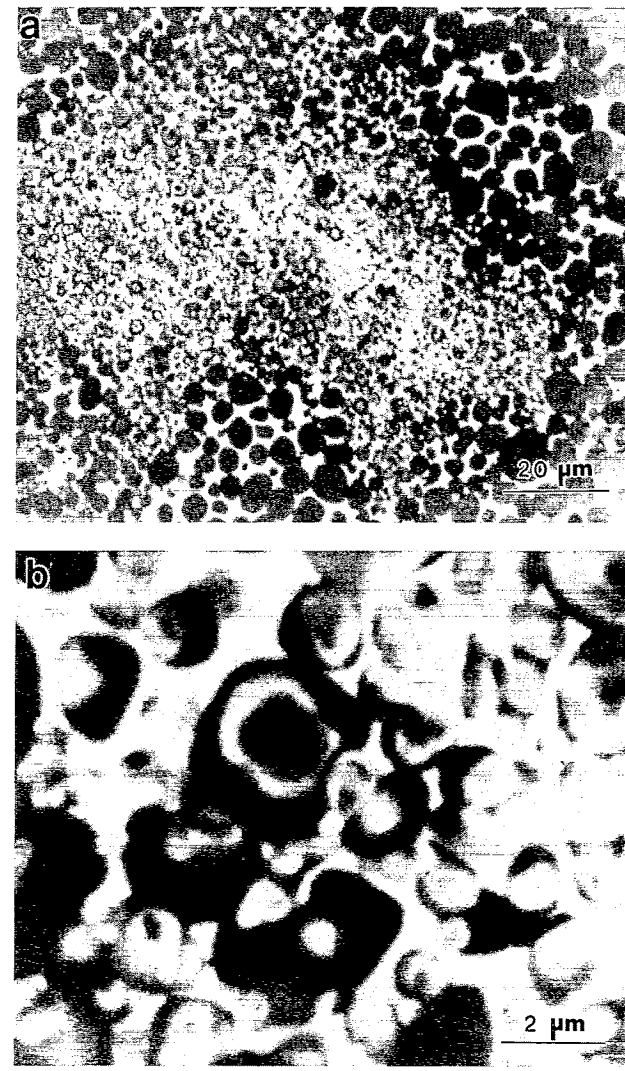

Fig. 6. (a) Mo-rich region found in the combustion synthesized–impact forged materials; (b) higher magnification revealing the core–shell type structure.

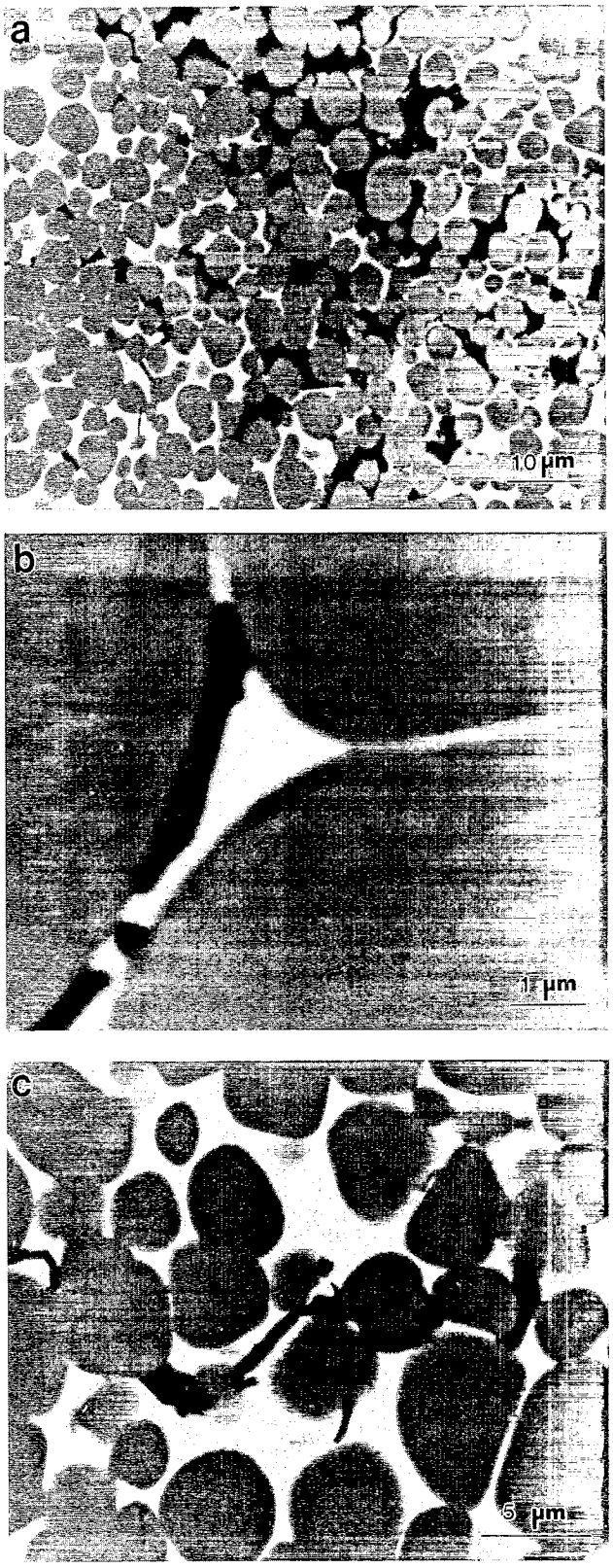

Fig. 7. Microstructural flaws observed within the 0 Mo material; (a) region devoid of Ni alloy binder; (b) interphase debonding; (c) partial interphase debonding and microcracks within the Ni alloy binder.

stresses in TiC–Ni cermets at temperatures up to 1100 °C, which were the result of the difference in the thermal expansion behavior between the two phases. It was determined that the carbide phase was essentially under isostatic compression while the Ni phase was under isostatic tension. The residual stress within the Ni phase at room temperature was estimated to be approximately 1100 MPa. The flaws shown in Fig. 7 are attributed to the partial wetting of the Ni alloy binder on the carbide phase. A carbide skeletal structure with increased rigidity following densification is formed (i.e. increased carbide contiguity). As the material cools, residual stresses due to thermal expansion differences are generated (tensile in the Ni alloy binder). This can then lead to interphase debonding and binder microcracks if the stresses are sufficiently large. Mo results in a decrease in carbide phase continuity and an increase in the interphase bond strength. This results in a less rigid carbide skeletal structure and consequently lower residual stresses.

3.2. Mechanical properties

The measured mechanical properties for the 0 Mo, 4 Mo, and 8 Mo materials are listed in Table 2. Also listed are the mean carbide particle sizes. Fracture toughness estimates were made possible from the transverse rupture strength measurements owing to the observation of failure-initiating flaws on the fracture surfaces. It is believed that the improvement in mechanical properties with increasing Mo content is mainly due to the increase in interphase bond strength and to the decrease in the number of microstructural flaws (supported by the microstructural observations above). A substantial increase in the transverse rupture strength between the 0 Mo and 8 Mo materials is obtained. The transverse rupture strength is extremely sensitive to pre-existing flaws. Overall, the mechanical properties for the 8 Mo material are comparable with those of conventionally produced cermets with similar compositions [29–33,41–44].

For the compositions investigated, the addition of Mo does not significantly affect the hardness. The indentation size (about 20 μm) was such that several carbide particles were deformed in each measurement. The mean Vickers microhardness of the specimens is approximately 13 GPa, which is equivalent to a Rockwell A hardness of about 87 [41].

Fig. 8 shows a typical stress–strain curve obtained for the 0 Mo composition material. The Young's modulus from this curve is approximately 200 GPa, which is much below the values listed in Table 2. This is due to the inherent difficulty in determining the specimen displacement for "stiff" elastic materials with the experimental set-up used in this investigation. The non-linear behavior prior to failure as indicated by the arrow in Fig. 8 was observed in all specimens tested. The non-linear behavior is due to the combined effects of plastic deformation of the Ni binder phase, microcracking, and interphase debonding.

Table 2
Summary of mechanical properties for the 0, 4, and 8 Mo materials

Mo content (wt.%)	0	4	8
Density (kg m^{-3})	5500	5730	6050
Mean particle size (μm)	4.57 ± 0.15	3.67 ± 0.12	4.35 ± 0.15
Vickers' hardness (GPa)	13.06 ± 1.59	12.97 ± 1.12	13.33 ± 1.39
Compressive strength (MPa)	2937 ± 110	3252 ± 112	3378 ± 87
Bend strength (MPa)	471 ± 95	815 ± 27	1326 ± 70
Fracture toughness (MPa m$^{1/2}$)	9 ± 1	11 ± 2	22 ± 1
Young's modulus (GPa)	311	321	340
Shear modulus (GPa)	120	123	131
Poisson's ratio	0.3	0.3	0.3
Longitudinal wave speed (m s^{-1})	8688 ± 54	8749 ± 56	8637 ± 54
Transverse wave speed (m s^{-1})	4644 ± 15	4631 ± 15	4659 ± 15

The mode I fracture toughness K_C values as a function of composition were calculated based on the observation of flaws on the fracture surfaces at which failure was initiated. The pre-existing flaw geometry for the 0 Mo and 4 Mo materials was semielliptical while that in the 8 Mo material was partial through thickness. The fracture toughness for a semielliptical flaw whose normal is oriented parallel to the transverse applied stress is given by [45]

$$K_{IC} = 2\sigma\left(\frac{a}{\pi}\right)^{1/2} \tag{4}$$

where σ is the failure stress and a is the depth of the flaw. The failure stress and depth of the flaw for the 0 Mo and 4 Mo materials were 575 MPa and 200 μm, and 773.5 MPa and 150 μm, respectively. The flaws were measured within the scanning electron microscope. The mode I fracture toughness for the partial-through-thickness geometry is given by [46]

$$K_I = \frac{R}{2wh^{1/2}} f\left(\frac{a}{h}\right) \tag{5a}$$

$$f\left(\frac{a}{h}\right) = \frac{3(L/h)(a/h)^{1/2}}{2(1+2a/h)(1-a/h)^{3/2}} \times \left\{1.99 - \frac{a}{h}\left(1-\frac{a}{h}\right) \times \left[2.15 - 3.93\frac{a}{h} + 2.7\left(\frac{a}{h}\right)^2\right]\right\} \tag{5b}$$

where w and h are the width and height of the four-point bend specimen, R is the maximum applied load, and $f(a/h)$ is a geometric factor which depends on the flaw size a and the height of the specimen. The parameters for this test were $R = 4886$ N, $w = 4.6 \times 10^{-3}$ m, $h = 7 \times 10^{-3}$ m, $a \approx 8.7 \times 10^{-4}$ m, and $f(a/h) = 3.38$. The plane strain fracture toughness K_{IC} for this crack geometry–loading combination is given by [45]

$$K_{IC} = 1.1\sigma(\pi a)^{1/2} \tag{6}$$

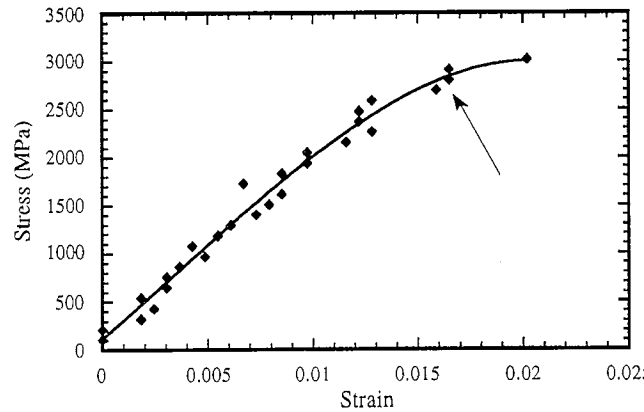

Fig. 8. Stress–strain curve for the 0 Mo composition. Note the non-linear deformation as indicated by the arrow.

Using the parameters above and $\sigma = 365$ MPa, the plane strain fracture toughness K_{IC} obtained is 21 ± 1 MPa m$^{1/2}$. The plane strain fracture toughness agrees well with the fracture toughness value calculated using Eq. (5a), indicating a small plastic zone at the crack tip in comparison with the specimen thickness.

The increase in the Young's and shear moduli with increasing Mo addition mainly reflects the decrease in the number of microstructural flaws such as microcracks and voids. The theoretical densities of the 0 Mo, 4 Mo, and 8 Mo materials are 5692 kg m^{-3}, 5831 kg m^{-3}, and 5977 kg m^{-3} respectively. These were calculated based on the densities of TiC (4930 kg m^{-3}), Ni (8900 kg m^{-3}), and Mo (10 200 kg m^{-3}). The percentages of theoretical density for the 0 Mo, 4 Mo, and 8 Mo materials are 97.5, 98.3, and 100. Assuming that the porosity is uniformly distributed as spherical microcavities throughout the body, then the expected decrease in the elastic moduli of the 0 Mo and 4 Mo materials due to these microcavities can be estimated. For a dilute distribution of microcavities in a linear elastic isotropic body, the effective Young's modulus is given by [47]

$$\frac{\bar{E}}{E} = 1 - 3f \tag{7}$$

where f is the cavity volume fraction (this result is actually for the in-plane Young's modulus of a body containing circular cylinders, i.e. transversely isotropic). For the 0 Mo and 4 Mo materials, the cavity volume fractions f are 0.025 and 0.017 respectively. If it is further assumed that the elastic moduli of the 8 Mo material represent the elastic moduli for fully dense 0 Mo and 4 Mo materials, then the decreases are 8.5% and 5.6% respectively. Based on Eq. (7), the estimated decreases for the 0 Mo and 4 Mo materials are 7.5% and 5.1% respectively. The Young's moduli degradation estimates agree reasonably well with the experimental data. This supports the idea that the elastic moduli enhancement due to the addition of Mo is mainly the result of an elimination of microstructural flaws.

3.3. Fracture morphology characterization

The fracture surface morphologies of the compression and bend specimens were basically the same. An exception to this was observed near the ends of the compression specimens. The fracture surfaces near the ends were often a darker shade of gray. The state of stress at the ends of the compression specimen is altered as a result of frictional end effects. Thus, near the ends of the specimen, the maximum principal tensile stress direction is oriented at an obtuse angle to the loading direction [34]. As a consequence, the fracture surfaces are oriented at an acute angle to the loading direction. Therefore, during failure the fracture surfaces rub over one another, causing the Ni alloy binder to "smear". This is shown in Fig. 9(a).

Away from the ends of the specimen, the failure mode was axial splitting (i.e. fracture surfaces perpendicular to the loading axis). This is shown in Fig. 9(b). The transgranular crack propagation mode is indicative of the relatively strong interphase bond.

Fig. 10 shows photographs from a crack within a 0 Mo specimen which did not propagate sufficiently to cause failure (loading axis is approximately top to bottom). Crack branching is clearly seen. Carbide particle fracture (arrows 1), interphase debonding (arrows 2), and microcracks within the Ni alloy binder (arrows 3) can be seen. Fig. 11 schematically illustrates the crack propagation mechanism assuming a strong interphase interfacial bond and no residual tensile strain within the metallic binder of carbide phase contiguity. Because the TiC phase is brittle ($K_{IC} = 2–3$ MPa $m^{1/2}$ [48]), crack initiation would be expected to occur in it first. As a result, more of the load is transferred to the surrounding Ni alloy binder. However, because the Ni alloy binder is tough ($K_{IC} > 100$ MPa $m^{1/2}$ [49]), it plastically deforms, forming thin ligaments which resist the propagation of the crack.

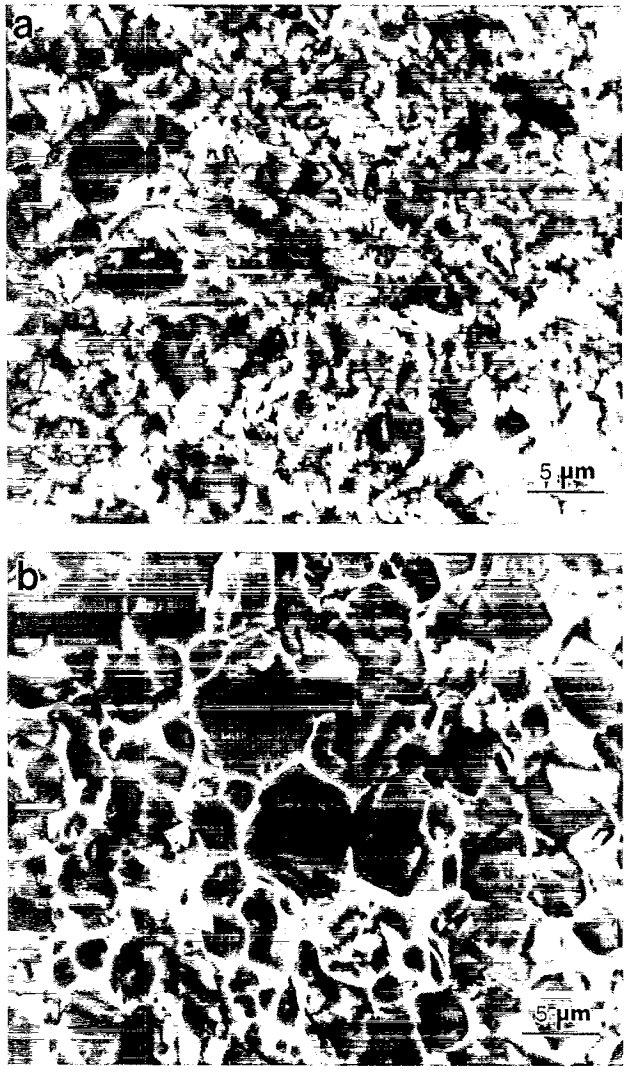

Fig. 9. (a) Fracture surface morphology near ends of specimen; (b) fracture surface morphology in central region of the specimen.

4. Summary and conclusions

For the compositions studied in this investigation, Mo was found to have a beneficial effect on the mechanical properties of TiC–Ni-based cermets produced by combustion synthesis–impact forging. The carbide particle size and particle size distribution were not strongly affected. The mean carbide particle size ranged between 3.5 and 4.5 μm, while the morphology was generally spheroidal with slight faceting. The carbide particle size distributions are characteristic of a coarsened microstructure. Qualitatively, the carbide phase contiguity decreased with increasing Mo content. The 0 Mo material was observed to contain a number of flaws: voids (regions devoid of the Ni alloy binder), interphase debonding, and binder microcracks. The voids and interphase debonding are attributed to the incomplete wetting behavior of the Ni alloy binder melt on the carbide phase. The interphase debonding and binder microcracks are evidence of the existence of large residual elastic tensile strains at the interphase

boundary and within the binder itself. These flaws drastically decreased with increasing Mo content, being non-existent within the 8 Mo material. As in conventionally produced materials, Mo was found preferentially within the carbide phase. Mo-rich regions due to incomplete dissolution of large Mo agglomerates were observed.

The Vickers microhardness seemed to be independent of the Mo content, being approximately 13 GPa. Compressive strength, bend strength, fracture toughness, Young's moduli, and shear moduli improved with increasing Mo content. The improvements are mainly attributed to the decrease in flaw density with increasing Mo content. However, increased interphase bond strength, decreasing residual stresses and carbide phase contiguity are also believed to make positive contributions. The mean values for the 8 Mo material are 3377 MPa, 1326 MPa, 22 MPa $m^{1/2}$, 340 GPa, 131 GPa.

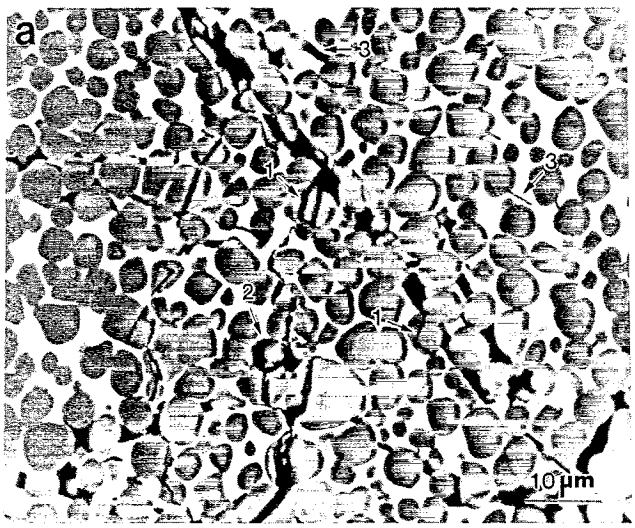

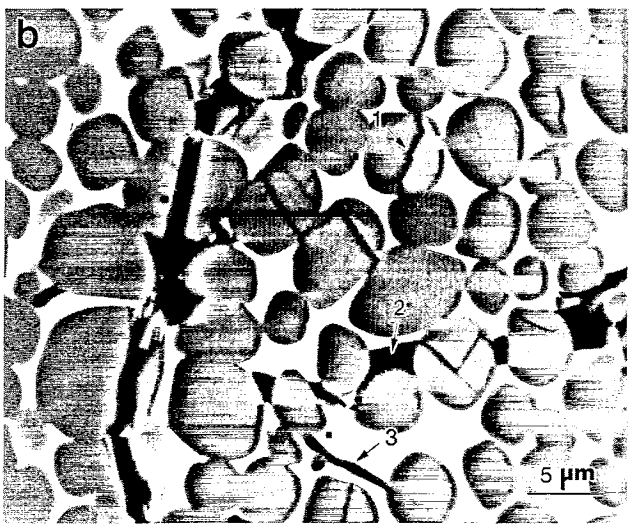

Fig. 10. (a), (b) Macrocrack with crack branching with a 0 Mo compression specimen. Carbide particle fracture (arrows 1), interphase debonding (arrows 2), and microcracks within the Ni alloy binder (arrows 3) can be seen.

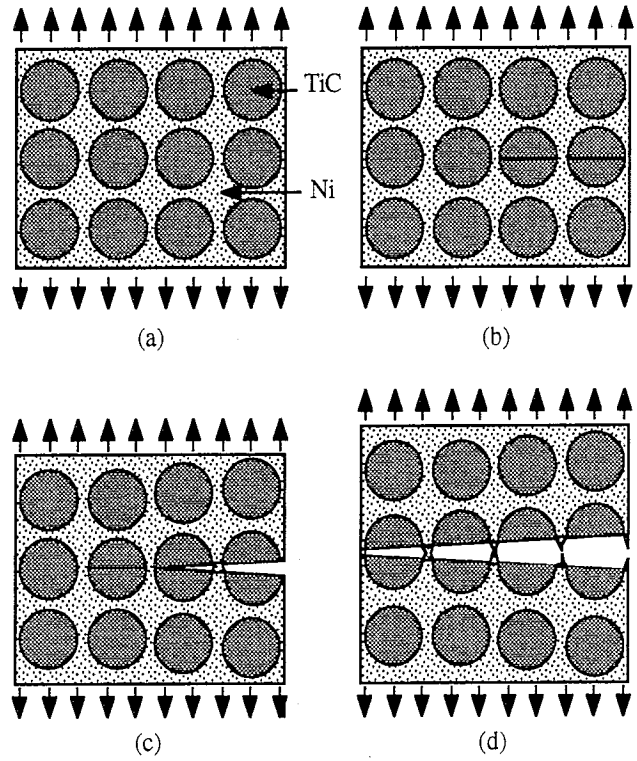

Fig. 11. Schematic illustration for crack propagation through cermet materials in which the interfacial bond strength is high: (a) application of load; (b) cracks form within the TiC particles as the load increases; (c) crack begins to open as Ni alloy binder deforms plastically; (d) Ni alloy "ligaments" rupture.

These are comparable with those of conventionally produced materials.

The fracture surface morphology was transgranular, indicative of strong interphase bonding. Fracture-initiating flaws on the four-point bend specimens' fracture surfaces enabled the estimation of their fracture toughness values.

Acknowledgements

This research was supported by the US Army Research Office under Contracts ARO-DAAL-03-88-K-0194 and ARO-DAAL-03-90-G-0204, and by the National Science Foundation under Grants DMR-8713258, DMR-9116570, and DMR-9396132. The authors would like to thank the continued support of Dr. E. Chen and Dr. A. Crowson of the US Army Research Office. Support by Dr. R. Skalak, Director of the Institute for Mechanics and Materials, is greatly appreciated.

References

[1] J.F. Crider, *Ceram. Eng. Sci. Proc.*, *3* (1982) 519.
[2] W.L. Frankhouser, K.W. Brendley, M.C. Kleszek and S.T. Sullivan, *Gasless Combustion Synthesis of Refractory Compounds*, Noyes, Park Ridge, NJ, 1985.

[3] Z.A. Munir and U. Anselmi-Tamburni, *Mater. Sci. Rep., 3* (1989) 277.
[4] H.C. Yi and J.J. Moore, *J. Mater. Sci., 25* (1990) 1159.
[5] A.G. Merzhanov, in Z.A. Munir and J.B. Holt (eds.), *Combustion and Plasma Synthesis of High Temperature Materials*, VCH, New York, 1990, p. 1.
[6] V. Hlavacek, *Am. Ceram. Soc. Bull., 70* (2) (1991) 240.
[7] I.P. Borovinskaya, E.A. Levashov and A.S. Rogachev, *Physical–Chemical and Technological Base of Self-Propagating High-Temperature Synthesis*, Scientific–Educational Center of SHS, Moscow, 1991.
[8] R.M. German, *Liquid Phase Sintering*, Plenum, New York, 1986.
[9] V.L. Kvanin, V.A. Gorovoi, N.T. Balikhina, I.P. Borovinskaya and A.G. Merzhanov, *Int. J. Self-Propag. High Temp. Synth., 2* (1) (1993) 56.
[10] Z.Y. Fu, W.M. Wang, H. Wang, R.Z. Yuan and Z.A. Munir, *Int. J. Self-Propag. High Temp. Synth. 2* (3) (1993) 307.
[11] V.V. Podlesov, A.V. Radugin, A.M. Stolin and A.G. Merzhanov, *J. Eng. Phys. Thermophys., 63* (5) (1993) 1065.
[12] E.E. Osipov, E.A. Levashov, V.N. Chernyshov, A.G. Merzhanov and I.P. Borovinskaya, *Int. J. Self-Propag. High Temp. Synth., 1* (2) (1992) 314.
[13] G.A. Adadurov, I.P. Borovinskaya, Yu. A. Gordopolov and A.G. Merzhanov, *J. Eng. Phys. Thermophys., 63* (5) (1993) 1166.
[14] Y. Miyamoto, M. Koizumi and O. Yamada, *J. Am. Ceram. Soc., 67* (11) (1984) *C*-224.
[15] H. Klemm, K. Tanihata and Y. Miyamoto, *J. Mater. Sci., 28* (1993) 1557.
[16] J.C. Murray and R.M. German, *Metall. Mater. Trans. A, 23* (1992) 2357.
[17] S.D. Dunmead, J.B. Holt and D.D. Kingman, in Z.A. Munir and J.B. Holt (eds.), *Combustion and Plasma Synthesis of High Temperature Materials*, VCH, New York, 1990, p. 186.
[18] S.D. Dunmead, Z.A. Munir, J.B. Holt and D.D. Kingman, *M. Mater. Sci., 26* (1991) 2410.
[19] R.V. Raman, S.V. Rele and M.J. Paskowitz, *J. Met., 45* (1) (1993) 54.
[20] J.C. LaSalvia, L.W. Meyer and M.A. Meyers, *J. Am. Ceram. Soc., 75* (3) (1992) 592.
[21] D.A. Hoke, M.A. Meyers, L.W. Meyer and G.T. Gray III, *Metall. Mater. Trans. A, 23* (1992) 77.
[22] J.C. LaSalvia, M.A. Meyers and D.K. Kim, *J. Mater. Synth. Process., 1* (2) (1994), 255.
[23] D.K. Kim, J.C. LaSalvia, D.A. Hoke and M.A. Meyers, *J. Am. Ceram. Soc.*, (1995), accepted.
[24] A. Niiler, L.J. Kecskes, T. Kottke, P.H. Netherwood, Jr. and R.F. Benck, *Ballistics Research Laboratory Rep. BRL-TR-2951.* December 1988, (Aberdeen Proving Ground, MD).
[25] B.H. Rabin, G.E. Korth and R.L. Williamson, *J. Am. Ceram. Soc., 73* (7) (1990) 2156.
[26] H.A. Grebe, A. Advani, N.N. Thadhani and T. Kottke, *Metall. Mater. Trans. A, 23* (1992) 2365.
[27] M. Humenik, Jr., and N.M. Parikh, *J. Am. Ceram. Soc., 39* (2) (1956) 60.
[28] N.M. Parikh and M. Humenik, Jr., *J. Am. Ceram. Soc., 40* (9) (1957) 315.
[29] J.R. Tinklepaugh and W.B. Crandall (*eds.*), *Cermets*, Reinhold, New York, 1960.
[30] D. Moskowitz and M. Humenik, Jr., in H.H. Hausner (eds.), *Modern Developments in Powder Metallurgy*, Vol. 3, Plenum, New York, 1966, p. 83.
[31] G.V. Samsonov, G.T. Dzodziev, L.I. Klyachko and V.K. Vityanyuk, *Sov. Powder Metall. Met. Ceram., 12* (4) (1972) 300.
[32] G.T. Dzodziev, A.A. Kal'kov, A.A. Dubrovskii, V.A. Gotlib, E.F. Korzukhina and T.A. Shapoval, *Sov. Powder Metall. Met. Ceram., 144* (4) (1983) 318.
[33] J.L. Ellis and C.G. Goetzel, in *Metals Handbook: Properties and Selection: Nonferrous Alloys and Special-Purpose Materials*, Vol. 2, ASM International, Metals Park, OH, 10th edn., 1990, p. 978.
[34] R.C. Lueth and T.E. Hale, *Mater. Res. Stand.*, (February 1970) 23.
[35] J. Blitz, *Fundamentals of Ultrasonics*, Butterworths, London, 1967.
[36] Y.C. Fung, *Foundations of Solid Mechanics*, Prentice-Hall, Englewood Cliffs, NJ, 1965.
[37] A.S. Rogachev, A.S. Mukas'yan and A.G. Merzhanov, *Dokl. Akad. Nauk SSSR, 297* (1987) 1240.
[38] J.C. LaSalvia, D.K. Kim, R.A. Lipsett and M.A. Meyers, *Metall. Mater. Trans. A, 26A*, 3001 (1995).
[39] D.R. Lide (ed.), *CRC Handbook of Chemistry and Physics*, CRC Press, Boston, MA, 1990.
[40] H.W. Newkirk, Jr., and H.H. Sisler, *J. Am. Ceram. Soc., 41* (3) (1958) 93.
[41] *Metals Handbook: Properties and Selection: Stainless Steels, Tool Materials, and Special Purpose Metals*, Vol. 3, ASM International, Metals Park, OH, 9th edn., 1978, p. 448.
[42] C.G. Goetzel, in *Metals Handbook: Powder Metallurgy*, Vol. 7, ASM International, Metals Park, OH, 9th edition, 1978, p. 798.
[43] G.T. Fisher II, L.L. Oden and G. Asai, *Bureau of Mines Rep. of Investigations, RI9115*, 1987 (US Department of the Interior).
[44] M. Loshak, N. Konovalenko, T. Shapoval and M. Dudkin, in J. Carlsson and N.G. Ohlson (eds.), *Mechanical Behaviour of Materials–IV, Proc. 4th Int. Conf.*, Vol. 2, Pergamon, Oxford, 1984, p. 865.
[45] R.W. Hertzberg, *Deformation and Fracture Mechanics of Engineering Materials*, Wiley, New York, 1983.
[46] T.L. Anderson, *Fracture Mechanics: Fundamentals and Applications*, CRC Press, Boston, MA, 1991.
[47] S. Nemat-Nasser and M. Hori, *Micromechanics: Overall Properties of Heterogeneous Materials*, North-Holland, Amsterdam, 1993.
[48] J.L. Chermant, A. Deschanvres and F. Osterstock, *Fract. Mech. Ceram., 4* (1978) 891.
[49] M.F. Ashby and D.R.H. Jones, *Engineering Materials: an Introduction to their Properties and Applications*, Pergamon, New York, 1980.